High-speed atomic force microscopy reveals rotary catalysis of rotor-less F1-ATPase

High-speed atomic force microscopy reveals rotary catalysis of rotor-less F_1-ATPase

Takayuki Uchihashi[1, 2, 3]*, Ryota Iino[3, 4, 5]*, Toshio Ando[1, 2, 3]‡, Hiroyuki Noji[3, 4, 5]‡

[1]Department of Physics, Kanazawa University, Kakuma-machi, Kanazawa 920-1192, Japan
[2]Bio-AFM Frontier Research Center, College of Science & Engineering, Kanazawa University, Kakuma-machi, Kanazawa 920-1192, Japan
[3]CREST, JST, Sanban-cho, Chiyoda-ku, Tokyo 102-0075, Japan
[4]Institute of Scientific and Industrial Research, Osaka University, Ibaraki, Osaka 567-0047, Japan
[5]Department of Applied Chemistry, School of Engineering, The University of Tokyo, Bunkyo-ku, Tokyo 113-8656, Japan

*These authors equally contributed to this work.

‡Corresponding authors:

Hiroyuki Noji, Professor
Department of Applied Chemistry, School of Engineering
The University of Tokyo
Bunkyo-ku, Tokyo 113-8656, Japan
Tel: +81-3-5841-7252, Fax: +81-3-5841-1872
E-mail: hnoji@appchem.t.u-tokyo.ac.jp

Toshio Ando, Professor
Department of Physics
Kanazawa University
Kakuma-machi, Kanazawa 920-1192, Japan
Tel: +81-76-264-5663, Fax: +81-76-264-5739
E-mail: tando@staff.kanazawa-u.ac.jp

One-sentence summary:
Intrinsic cooperativity engenders cyclical propagation of conformational states in the stator ring of an ATP-driven rotary motor.

ABSTRACT

F_1 is an ATP-driven motor in which three torque-generating β subunits in the $\alpha_3\beta_3$ stator ring sequentially undergo conformational changes upon ATP hydrolysis to rotate the central shaft γ unidirectionally. Although extensive experimental and theoretical work has been done, the structural basis of cooperative torque generation to realize the unidirectional rotation remains elusive. We use high-speed atomic force microscopy to show that the rotor-less F_1 still "rotates"; in the isolated $\alpha_3\beta_3$ stator ring, the three β subunits cyclically propagate conformational states in the counterclockwise direction, similar to the rotary shaft rotation in F_1. The structural basis of unidirectionality is programmed in the stator ring. These findings have implications for cooperative interplay between subunits in other hexameric ATPases.

F_1-ATPase, a water-soluble portion of ATP synthase (*1*), is a rotary motor protein. The $\alpha_3\beta_3\gamma$ subcomplex (referred to here as F_1) suffices as the motor, in which the rotor γ subunit rotates in the stator $\alpha_3\beta_3$ ring upon ATP hydrolysis (*2*). The concept of the "rotary catalysis" of F_1 was proposed based on biochemical studies (*3*). It was strongly supported by the first crystal structure (*4*) and directly proven by observations of rotating single molecules (*5*). In F_1, the catalytic sites are located at the α-β interfaces, mainly on the β subunits. In the crystal structure (*4*), three catalytic sites are in different nucleotide-bound states; one binds to an ATP analog (α_{TP}-β_{TP} in Fig. 1E), another binds to ADP (α_{DP}-β_{DP}), and the third is unbound (α_E-β_E). Both β_{TP} and β_{DP} assume the closed conformation, swinging the C-terminal domain toward γ, whereas β_E assumes the open conformation, swinging the domain away from γ. As these two general conformational states appear to push or be pushed by γ, respectively, it was proposed that interactions with γ control the conformational and catalytic states of individual βs to sequentially generate torque (*6*). In fact, some biochemical studies are thought to suggest that the $\alpha_3\beta_3$ ring alone does not possess intrinsic cooperativity and γ mediates the interplay among βs (*7-9*). This view was reinforced by studies showing that backward mechanical rotation of γ with external force reverses the chemical reaction toward ATP synthesis (*10, 11*), whereas forced forward rotation results in accelerated ATP binding (*12*).

Recently, however, this contention has been challenged by the finding that even when most interaction sites between β and γ are abolished, F_1 retains catalytic power to rotate γ unidirectionally (*13, 14*). A few biochemical studies also suggest the intrinsic cooperativity of the $\alpha_3\beta_3$ ring (*15, 16*). However, as conventional single-molecule optical microscopy requires attachment of a probe onto the rotary shaft for visualization (*5*), it does not allow direct examination of whether the intrinsic cooperativity in the $\alpha_3\beta_3$ ring is the core feature responsible for sequential torque generation. Here we clarified this issue by directly imaging the ATP-driven conformational transition of βs in the isolated $\alpha_3\beta_3$ ring using high-speed atomic force microscopy (AFM) (*17, 18*), a technique that can visualize proteins at work in real time without probes (*19, 20*).

The $\alpha_3\beta_3$ subcomplex (Fig. S1, Supporting Online Materials (SOM)) was covalently immobilized on a mica surface, and observed with high-speed AFM with frame capture time of 80 ms unless otherwise mentioned (Fig. 1, Fig. S2, S3). In the absence of nucleotide, the $\alpha_3\beta_3$ showed a pseudo-six-fold symmetric ring in which alternately arranged three subunits were elevated relative to the other three (Fig. 1A, Fig. S4). The simulated AFM image of the C-terminus side of the ring constructed from the crystal structure of the nucleotide-free $\alpha_3\beta_3$ subcomplex (*21*) well reproduced the observed image (Fig. 1C). This indicates that the N-terminus side was selectively

attached to the mica, although a smaller ring corresponding to the N-terminus side was occasionally observed (Fig. S5). The three βs, which all assumed an open conformation in the crystal structure of $\alpha_3\beta_3$, gave three protruding peaks in the simulated image as bright spots. When a non-hydrolyzable ATP analog AMPPNP was added, the ring became triangular and the central hole was obscured (Fig. 1D). Although the three αs with lower protrusions retained the same conformation as those under the nucleotide-free condition, two of three βs retracted towards the center and simultaneously lowered their protrusions. Consequently, the ring showed a single high protrusion. A simulated image of $\alpha_3\beta_3$ with bound nucleotides was constructed using a structure in which γ was removed from the crystal structure of F_1 (Fig. 1E) (*4*). The simulated image (Fig. 1F) also showed an asymmetric ring very similar to that of the observed image. The excellent agreement indicates that only two βs can assume the closed conformation, even in saturating AMPPNP. This feature is consistent with the observation that three βs do not assume the closed conformation simultaneously (*22*).

When ATP was added, β showed distinct conformational dynamics; each β underwent a conformational transition between the outwardly extended high state (open) and the retracted low state (closed) (Fig. 2A, Table S1); the outwardly extended and retracted conformations correlated well with the high and low protrusion states,

respectively (Fig. S6). The most prominent features are that only a single β assumes the open state, as in the presence of AMPPNP, and that when the open-to-closed transition occurs at one β, the opposite closed-to-open transition occurs simultaneously at its counterclockwise neighbor β in most cases. Thus the high and outwardly extended conformation propagates in the counterclockwise direction (Fig. 2A and 2B).

For a more quantitative analysis of this cooperativity, the conformational states of the three βs in each image frame were determined from their correlation coefficients using respective reference images of βs in the open state (Fig. S7, SOM). The correlation coefficients are distributed around two distinct peaks at ~0.995 and ~0.96 (Fig. 2C). The peaks with larger and smaller coefficients correspond to the open (O) and closed (C) states, respectively. On the other hand, the correlation coefficient analysis for the nucleotide-free and AMPPNP-bound $\alpha_3\beta_3$ showed static conformations of β (Fig. S8 and S9, Table S1). Fig. 2D shows typical time courses of the two conformational states for individual βs. In all images observed in the presence of 2–4 μM ATP (n = 8746), three βs at a given frame dominantly showed the "CCO" state (82% of total). The COO state was also observed (14.5%). Other states such as CCC (3%) and OOO (0.5%) were rare. We analyzed the rotary propagation of the O and C states by counting the number of counterclockwise shifts of the CCO state (Fig. 2E, SOM). The propagation is

unidirectional, rotating counterclockwise with an efficiency of 83% (in 2 μM ATP) over the total shift events examined (n = 371) (see also Fig. S10). Considering that two consecutive counterclockwise shifts occurring occasionally within the frame capture time (80 ms) would be counted as a clockwise shift, this value of efficiency is likely underestimated by ~6% (Fig. 3D, Fig. S11, SOM).

The rate of rotational propagation of the CCO state increased with increasing ATP concentration (Fig. 3A-C), indicating that ATP binding is rate-limiting, consistent with the biochemically determined K_m of 12 μM for ATP hydrolysis (Fig. S1). Histograms of the dwell time of the O state followed a single exponential function, and those of the C state were well fitted with the model that two consecutive events of ATP binding to the other two βs trigger the transition of the β from the C to the O state (Fig. S11). The rate constants of the counterclockwise shift of the CCO state were comparable with the initial rates of ATP hydrolysis measured biochemically (Fig. 3D). Thus, each ATP hydrolysis is well coupled with the open-to-close transition of β. Just before transitioning to the next CCO state, a COO state occasionally appeared (~30% of total transitions) (christcrosses in Fig. 2E, Fig. 3A-C). In this event, one of the two closed βs positioned at the counterclockwise side opened in most cases, implying that ADP can be released from the closed β before ATP binds to the open β (*23*, *24*).

The present results prove that the stator $\alpha_3\beta_3$ ring alone possesses high cooperativity for sequential power stroking among three catalytic βs. This was also indicated by the observations that the occasional subunit dissociation completely stopped the rotary propagation of conformational state (Fig. S12). Thus, the "γ-dictator" model (*13*), which proposes that only the interaction with γ determines the conformational and catalytic states of βs (*23, 24*), is not valid. On the other hand, ATP-binding rate and the efficiency of unidirectionality of the $\alpha_3\beta_3$ subcomplex are distinctly lower than those of F_1 (Fig. 3, Fig. S11). Thus, the interaction with γ is dispensable but still important for the rapid and precise rotary catalysis. Our findings are not inconsistent with the observations that the rates and equilibriums of the catalytic reactions are apparently under the control of the rotary angle of γ (*10-12*). The intrinsic interplay among βs would reinforce catalytic control by γ; even if γ tightly interacts with only one β, it still can act on all βs through β-β interplay.

These results also have implications for the cooperativity of other structurally-related hexameric ATPases such as RecA- and AAA+-family proteins in which cooperativity among the separate catalytic sites is a central issue (*25*). These ATPases may also have intrinsic cooperativity. Comparative studies on these proteins should shed light on the common operating principles of hexameric ATPases.

REFERENCES AND NOTES

1. P. D. Boyer, The ATP synthase – a splendid molecular machine. *Annu Rev Biochem* **66**, 717 (1997).

2. W. Junge, H. Sielaff, S. Engelbrecht, Torque generation and elastic power transmission in the rotary FOF1-ATPase. *Nature* **459**, 364 (2009).

3. M. J. Gresser, J. A. Myers, P. D. Boyer, Catalytic site cooperativity of beef heart mitochondrial F1 adenosine triphosphatase. Correlations of initial velocity, bound intermediate, and oxygen exchange measurements with an alternating three-site model. *J Biol Chem* **257**, 12030 (1982).

4. J. P. Abrahams, A. G. Leslie, R. Lutter, J. E. Walker, Structure at 2.8 A resolution of F1-ATPase from bovine heart mitochondria. *Nature* **370**, 621 (1994).

5. H. Noji, R. Yasuda, M. Yoshida, K. Kinosita, Jr., Direct observation of the rotation of F1-ATPase. *Nature* **386**, 299 (1997).

6. H. Wang, G. Oster, Energy transduction in the F1 motor of ATP synthase. *Nature* **396**, 279 (1998).

7. C. Kaibara, T. Matsui, T. Hisabori, M. Yoshida, Structural asymmetry of F1-ATPase caused by the gamma subunit generates a high affinity nucleotide binding site. *J Biol Chem* **271**, 2433 (1996).

8. J. J. Garcia, R. A. Capaldi, Unisite catalysis without rotation of the gamma-epsilon domain in Escherichia coli F1-ATPase. *J Biol Chem* **273**, 15940 (1998).

9. R. K. Nakamoto, C. J. Ketchum, M. K. al-Shawi, Rotational coupling in the F0F1 ATP synthase. *Annu Rev Biophys Biomol Struct* **28**, 205 (1999).

10. H. Itoh *et al.*, Mechanically driven ATP synthesis by F1-ATPase. *Nature* **427**, 465 (2004).

11. Y. Rondelez *et al.*, Highly coupled ATP synthesis by F1-ATPase single molecules. *Nature* **433**, 773 (2005).

12. Y. Iko, K. V. Tabata, S. Sakakihara, T. Nakashima, H. Noji, Acceleration of the ATP-binding rate of F1-ATPase by forcible forward rotation. *FEBS Lett* **583**, 3187 (2009).

13. S. Furuike *et al.*, Axle-less F1-ATPase rotates in the correct direction. *Science* **319**, 955 (2008).

14. N. Mnatsakanyan, A. M. Krishnakumar, T. Suzuki, J. Weber, The role of the betaDELSEED-loop of ATP synthase. *J Biol Chem* **284**, 11336 (2009).

15. M. Yoshida, W. S. Allison, The ATPase activity of the alpha 3 beta 3 complex of the F1-ATPase of the thermophilic bacterium PS3 is inactivated on modification

of tyrosine 307 in a single beta subunit by 7-chloro-4-nitrobenzofurazan. *J Biol Chem* **265**, 2483 (1990).

16. P. Aloise, Y. Kagawa, P. S. Coleman, Comparative Mg(2+)-dependent sequential covalent binding stoichiometries of 3'-O-(4-benzoyl)benzoyl adenosine 5'-diphosphate of MF1, TF1, and the alpha 3 beta 3 core complex of TF1. The binding change motif is independent of the F1 gamma delta epsilon subunits. *J Biol Chem* **266**, 10368 (1991).

17. T. Ando *et al.*, A high-speed atomic force microscope for studying biological macromolecules. *Proc Natl Acad Sci U S A* **98**, 12468 (2001).

18. T. Ando, T. Uchihashi, T. Fukuma, High-speed atomic force microscopy for nano-visualization of dynamic biomolecular processes. *Prog. Surf. Sci.* **83**, 337 (2008).

19. M. Shibata, H. Yamashita, T. Uchihashi, H. Kandori, T. Ando, High-speed atomic force microscopy shows dynamic molecular processes in photoactivated bacteriorhodopsin. *Nat Nanotechnol* **5**, 208 (2010).

20. N. Kodera, D. Yamamoto, R. Ishikawa, T. Ando, Video imaging of walking myosin V by high-speed atomic force microscopy. *Nature* **468**, 72 (2010).

21. Y. Shirakihara *et al.*, The crystal structure of the nucleotide-free alpha 3 beta 3

subcomplex of F1-ATPase from the thermophilic Bacillus PS3 is a symmetric trimer. *Structure* **5**, 825 (1997).

22. R. I. Menz, J. E. Walker, A. G. Leslie, Structure of bovine mitochondrial F(1)-ATPase with nucleotide bound to all three catalytic sites: implications for the mechanism of rotary catalysis. *Cell* **106**, 331 (2001).

23. K. Adachi *et al.*, Coupling of rotation and catalysis in F(1)-ATPase revealed by single-molecule imaging and manipulation. *Cell* **130**, 309 (2007).

24. R. Watanabe, R. Iino, H. Noji, Phosphate release in F1-ATPase catalytic cycle follows ADP release. *Nat Chem Biol* **6**, 814 (2010).

25. E. J. Enemark, L. Joshua-Tor, On helicases and other motor proteins. *Curr Opin Struct Biol* **18**, 243 (2008).

26. S. Sakakihara, S. Araki, R. Iino, H. Noji, A single-molecule enzymatic assay in a directly accessible femtoliter droplet array. *Lab Chip* **10**, 3355 (2010).

27. T. R. Rodriguez, R. Garcia, Theory of Q control in atomic force microscopy. *Appl. Phys. Lett.* **82**, 4821 (2003).

28. M. Wendel, H. Lorenz, J. P. Kotthaus, Sharpened electron beam deposited tips for high resolution atomic force microscope lithography and imaging. *Appl. Phys. Let.* **67**, 3732 (1995).

ACKNOWLEDGEMENTS

We thank M. Tanigawara, H. Yamashita, R. Hasegawa, and D. Okuno for technical help and members of the Noji and Ando laboratories for valuable comments. This work was supported by Grants-in-aid for Scientific Research from MEXT (Project ID# 18074005, 18201025, 21770168, 21681017, 2102301 and 20221006), the Knowledge Cluster Initiative, and the Japan Science and Technology Agency for Core Research for Evolutional Science and Technology.

FIGURE LEGENDS

Fig. 1. (A) Averaged AFM image of C-terminal side of the $\alpha_3\beta_3$ subcomplex without nucleotide (Online movie S1). (B) C-terminal side of crystal structure of the nucleotide-free $\alpha_3\beta_3$ subcomplex (PDB code: 1SKY) (*21*). The α and β subunits are colored in cyan and pink, respectively. The C-terminal DELSEED motif of β corresponding to the high protruding portions is highlighted in red. (C) Simulated AFM image of the $\alpha_3\beta_3$ subcomplex constructed from the structure in (B). (D) Averaged AFM image of C-terminal side of the $\alpha_3\beta_3$ subcomplex in 1 mM AMPPNP. (E) Atomic structure of the $\alpha_3\beta_3$ subcomplex with bound nucleotides. This structure is obtained by removing γ from the crystal structure of F_1 (PDB code: 1BMF) (*4*). (F) Simulated AFM image constructed from the structure in (E). The brightness of all AFM images in this paper represents the sample height but is not linearly set to highlight the top surface structure (Fig. S4).

Fig. 2. (A) Successive AFM images showing conformational change of βs in 2 μM ATP (Online movie S3). The highest pixel in each image is indicated by the red circle. Frame rate, 12.5 frames/s. (B) Time evolution of cumulated angle of highest pixel. The inset shows a trajectory, superimposed on an AFM image, of the highest pixels corresponding

to the high protrusions of open βs (412 frames, Online movie S6). The center of rotation is defined by the averaged x- and y-positions of the highest pixels, and the cumulated angles are calculated relative to the first frame. (C) Correlation coefficient histograms calculated for each β designated in (A) (n = 220). An open β is used as a reference for the analysis of each β. (D) Time courses of correlation coefficients. The white and grey backgrounds show periods of O and C states, respectively. Solid lines show the mean correlation coefficient for each period. (E) Time evolution of cumulated number of counterclockwise shifts of the CCO state. Circles, christcrosses, and crosses correspond to CCO, COO, and other irregular states (OOO and CCC), respectively. The increase in the cumulated number indicates that the open β in CCO shifts counterclockwise.

Fig. 3. (A-C) Time evolutions of cumulated number of counterclockwise CCO shifts at various concentrations of ATP ([ATP]). At each [ATP], four representative curves for the different molecules are indicated as in Fig. 2E. (D) [ATP] dependence of the initial rates of ATP hydrolysis determined by biochemical assay (circles; 2 μM, 1.6 ± 0.9 s^{-1}; 3 μM, 2.5 ± 1.0 s^{-1}; 4 μM, 3.3 ± 1.3 s^{-1} (Mean ± SD, n = 6)) and the rates of conformational change of β determined by fitting the dwell time histograms of open (squares; 2 μM, 1.5 s^{-1}; 3 μM, 3.0 s^{-1}; 4 μM, 3.8 s^{-1}) and closed (triangles; 2 μM, 1.5 s^{-1}; 3 μM, 2.5 s^{-1}; 4 μM,

3.2 s^{-1}) states shown in Fig. S11.

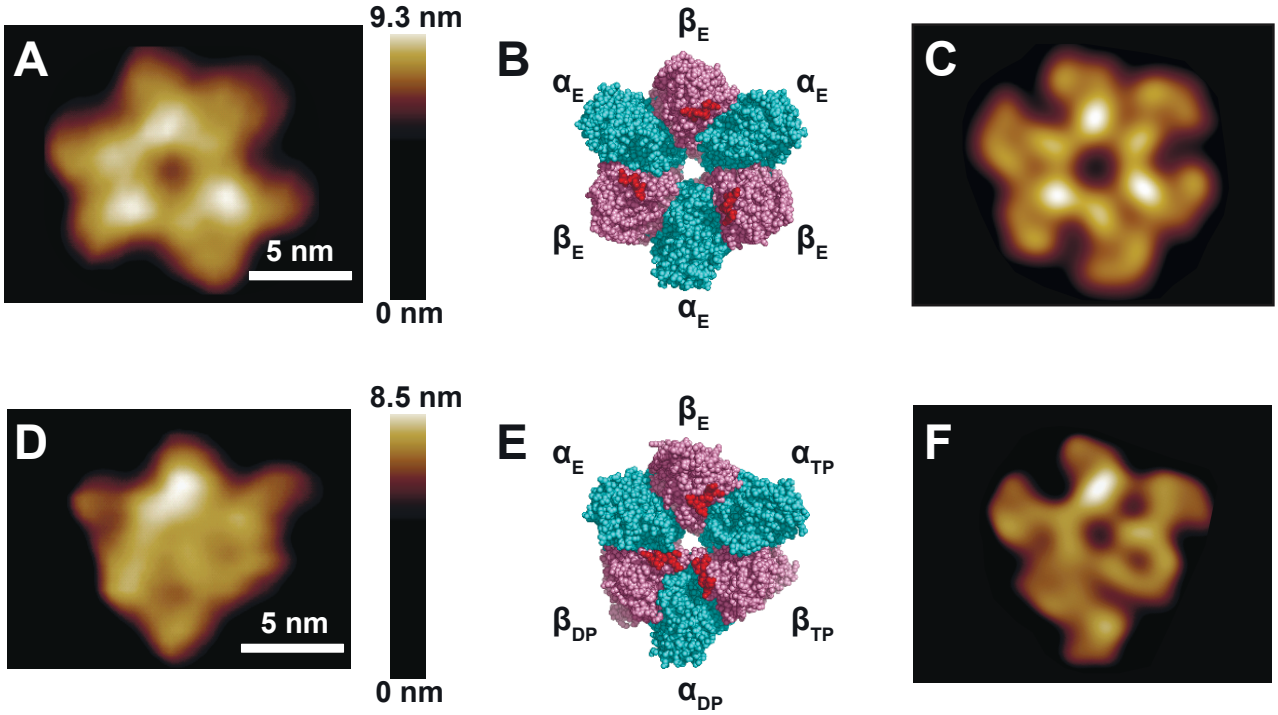
A
9.3 nm
5 nm
0 nm
B
β_E
α_E
α_E
β_E
β_E
α_E
C
D
8.5 nm
5 nm
0 nm
E
β_E
α_E
α_{TP}
β_{DP}
β_{TP}
α_{DP}
F

Fig. 1

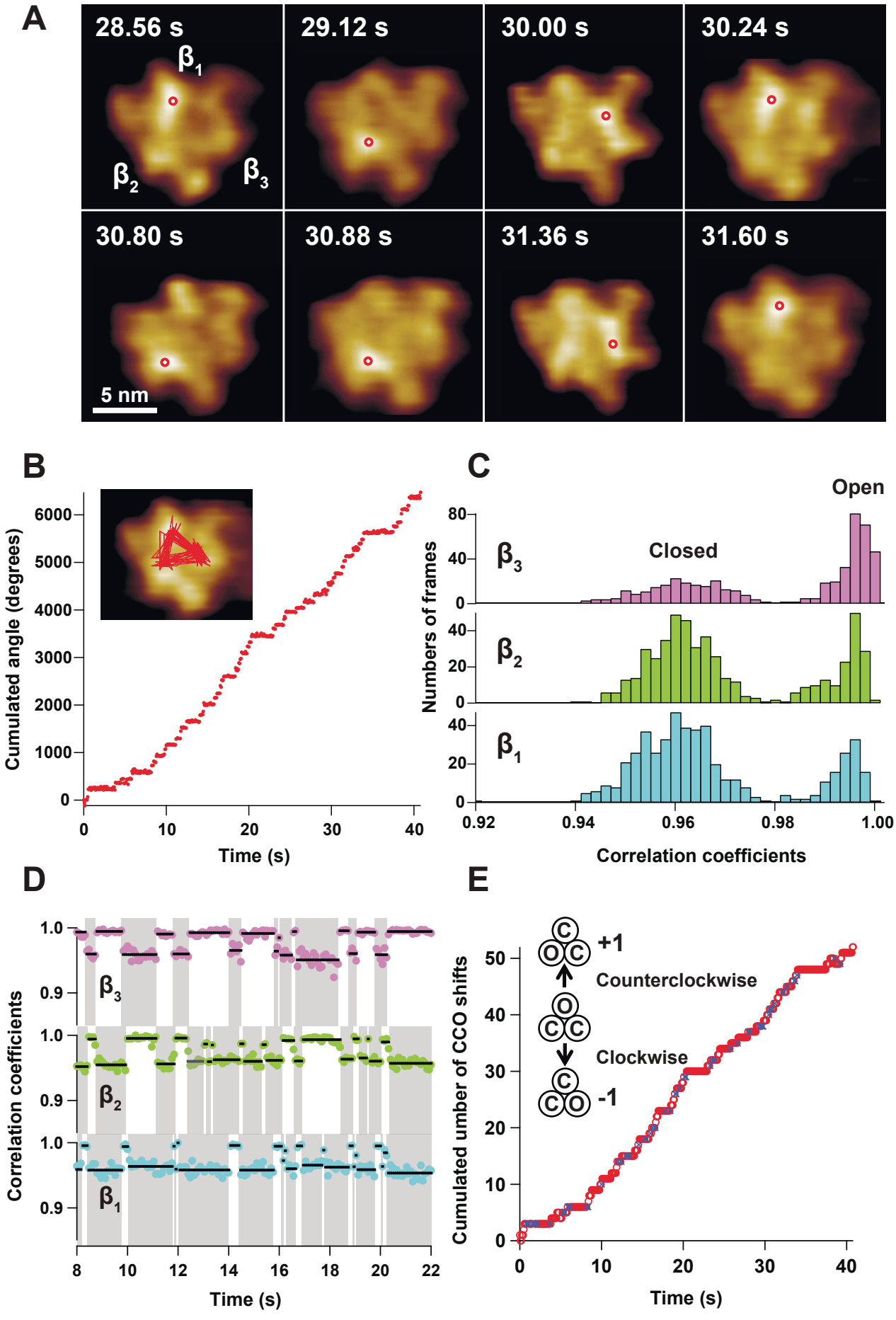
A
28.56 s
β1
β2
β3
29.12 s
30.00 s
30.24 s
30.80 s
30.88 s
31.36 s
31.60 s
5 nm
B
Cumulated angle (degrees)
6000
5000
4000
3000
2000
1000
0
0
10
20
30
40
Time (s)
C
Open
Closed
β3
β2
β1
Numbers of frames
80
40
0
40
20
0
40
20
0
0.92
0.94
0.96
0.98
1.00
Correlation coefficients
D
Correlation coefficients
1.0
0.9
1.0
0.9
1.0
0.9
β3
β2
β1
8
10
12
14
16
18
20
22
Time (s)
E
Cumulated umber of CCO shifts
50
40
30
20
10
0
0
10
20
30
40
Time (s)
+1
Counterclockwise
Clockwise
-1

Fig. 2

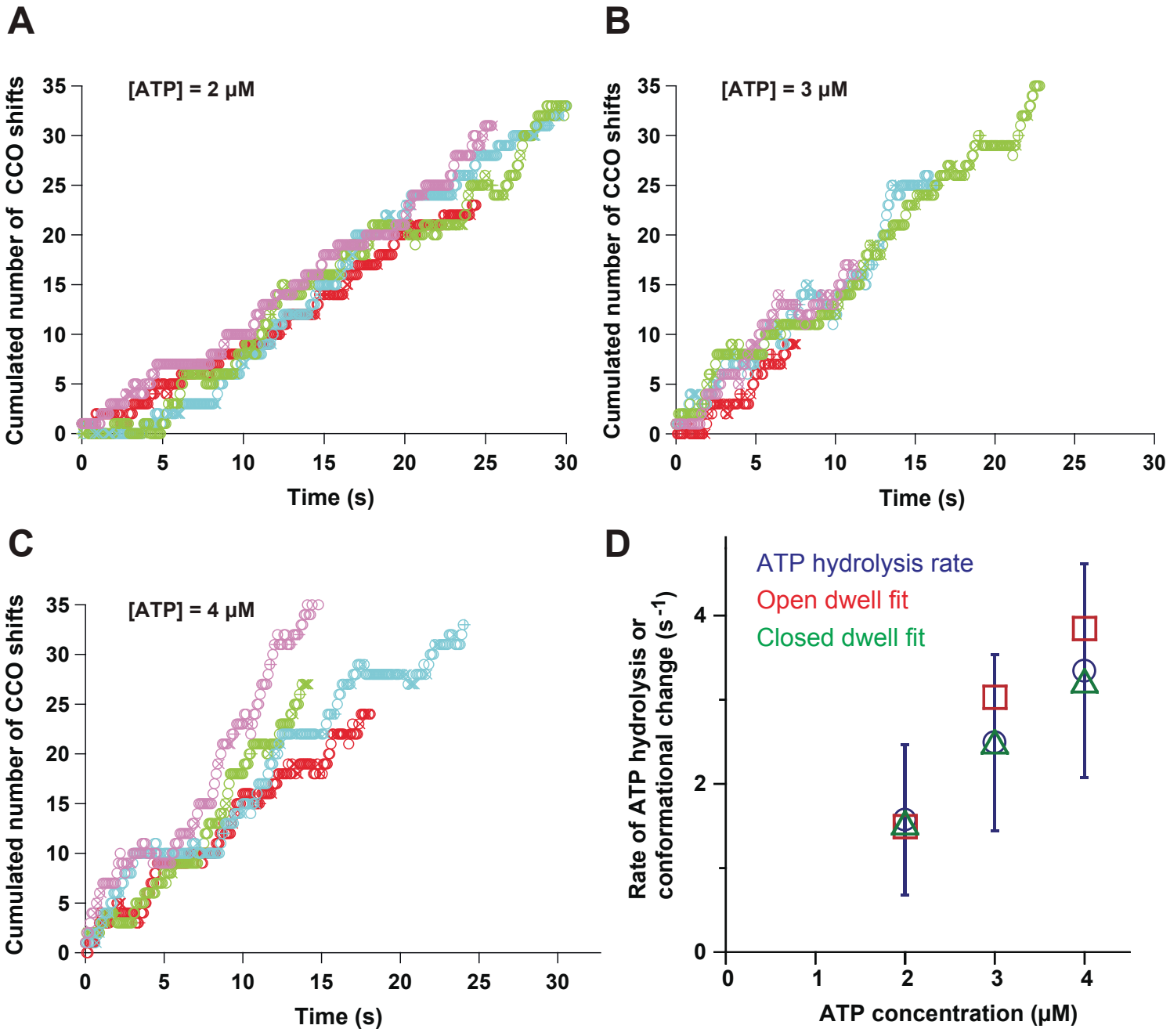
A
[ATP] = 2 μM
Cumulated number of CCO shifts
Time (s)
B
[ATP] = 3 μM
Cumulated number of CCO shifts
Time (s)
C
[ATP] = 4 μM
Cumulated number of CCO shifts
Time (s)
D
ATP hydrolysis rate
Open dwell fit
Closed dwell fit
Rate of ATP hydrolysis or conformational change (s-1)
ATP concentration (μM)

Fig. 3

Supporting Online Materials

High-speed atomic force microscopy reveals rotary catalysis of rotor-less F_1-ATPase

Takayuki Uchihashi, Ryota Iino, Toshio Ando, Hiroyuki Noji

MATERIALS AND METHODS

SUPPORTING FIGURES S1 TO S12

S11: Histograms of dwell times for the O and C states in various [ATP]

S12: Loss of a single subunit stops rotary propagation of conformational changes

SUPPORTING TABLE S1

S1: Fraction of molecules showing conformational changes in various nucleotide conditions.

SUPPORTING ONLINE MOVIES S1 TO S8

Movie S1: AFM movie of the C-terminal side of $\alpha_3\beta_3$ without nucleotide. Scan area, 18 × 15 nm^2; frame rate, 10 fps.

Movie S2: AFM movie of the N-terminal side of $\alpha_3\beta_3$ without nucleotide. Scan area, 17 × 11 nm^2; frame rate, 10 fps.

Movie S3: AFM movie of the C-terminal side of $\alpha_3\beta_3$ in 2 μM ATP. Scan area, 17 × 13 nm^2; frame rate, 12.5 fps.

Movie S4: AFM movie of the C-terminal side of $\alpha_3\beta_3$ in 3 μM ATP. Scan area, 18 × 14 nm^2; frame rate, 12.5 fps.

Movie S5: AFM movie of the C-terminal side of $\alpha_3\beta_3$ in 4 μM ATP. Scan area, 17 × 11 nm^2; frame rate, 12.5 fps.

Movie S6: AFM movie of the C-terminal side of $\alpha_3\beta_3$ in 2 μM ATP. Scan area, 21 × 14 nm^2; frame rate, 12.5 fps. The pixel with the highest (brightest) position in each image is indicated by the blue circle. The center used for calculating the rotational angle is indicated by the cross mark.

Movie S7: AFM movie of the C-terminal side of $\alpha_3\beta_3$ in 2 μM ATP. Scan area, 21 × 14 nm^2; frame rate, 12.5 fps. At 16 s, one β subunit was lost.

Movie S8: AFM movie of the C-terminal side of $\alpha_3\beta_3$ in 2 μM ATP. Scan area, 25 × 14 nm^2; frame rate, 12.5 fps. At 9 s, one α subunit was lost.

MATERIALS AND METHODS

Purification of $\alpha_3\beta_3$ subcomplex and measurement of ATP hydrolysis rate

The $\alpha(His_6$ at N-terminus/C193S$)_3\beta(His_3$-Lys_7 at N-terminus$)_3$ subcomplex of the F_1-ATPase from thermophilic *Bacillus sp.* PS3 was expressed in *E. coli*, and purified using Ni^{2+}-NTA affinity chromatography and size exclusion chromatography as described previously for purification of the $\alpha_3\beta_3\gamma$ subcomplex (*26*) (Fig. S1). The nucleotide-free $\alpha_3\beta_3$ subcomplex was stable and stored at room temperature before use. The ATP hydrolysis rate was measured with an ATP regenerating system using a UV-visible spectrophotometer (VP-550, Jasco). Various concentrations of ATP were added to the assay mixture (10 mM Tris-HCl (pH 8.0), 2 mM $MgCl_2$, 250 mM KCl, 2.5 mM phosphoenolpyruvate, 0.1 mg/ml pyruvate kinase, 0.1 mg/ml lactate dehydrogenase, and 0.2 mM NADH) at 0 s, followed by the addition of $\alpha_3\beta_3$ (final 30 nM) at 200 s. The NADH absorbance at 340 nm was monitored and the initial rate of ATP hydrolysis was calculated from the initial slope (for 10 s after the addition of $\alpha_3\beta_3$) of the change in [NADH] using a molecular extinction coefficient of 6,220. Measurements were carried out at 24–25 °C (Fig. S1).

Fixation of $\alpha_3\beta_3$ subcomplex onto substrate for AFM observation

To fix the $\alpha_3\beta_3$ subcomplex onto a mica substrate, we first treated the mica surface with 3-aminopropyl-triethoxysilane (0.05–0.1%) for 3 min and washed the surface with pure water. The mica was then treated with glutaraldehyde (0.1–0.25%) for 3 min and carefully washed with buffer A (10 mM HEPES-NaOH (pH 7.4), 10 mM KCl, 5 mM $MgSO_4$). A droplet containing the $\alpha_3\beta_3$ subcomplex (1–10 nM) was deposited on the surface for 5 min, which was then washed with buffer B (10 mM Tris-HCl (pH 8.0), 2 mM $MgCl_2$). The sample stage was mounted on the AFM head and immersed in buffer B with or without ATP or AMPPNP. AFM imaging showed that the $\alpha_3\beta_3$ subcomplex was strongly adsorbed on the mica surface by chemical cross-linking between the primary amine on the aminosilane-modified mica and the ε-amines of the lysine residues in the N-terminus of the β subunit. Judging from the observed images and height of the molecules (~9 nm), almost all molecules appeared to be adsorbed on the mica at either the C- or N-terminal side. Most (~70%) of the adsorbed molecules had the C-terminal side facing upward, whereas the rest had the N-terminal side facing upward. On bare and untreated mica surfaces, all molecules rapidly diffused on the surface and could not be imaged clearly.

High-speed AFM apparatus

We used a home-built high-speed AFM apparatus (*17*, *18*). The cantilevers (Olympus) were 6–7 μm long, 2 μm wide, and 90 nm thick. Their spring constant was 0.1–0.2 N/m, and their resonant frequency and quality factor in an aqueous solution were 0.7–1 MHz and ~2, respectively. For AFM imaging, the free oscillation amplitude was ~1 nm and the set-point amplitude was around 90% of the free oscillation amplitude. The tapping force estimated was less than 30 pN (*27*). An amorphous carbon tip was grown on the original tip by electron beam deposition (*28*). The tip length was adjusted to ~1 μm. The tip was sharpened by plasma etching under argon gas (tip apex, ~4 nm in radius).

AFM imaging and image processing

All AFM observations were performed at room temperature (24–26 °C). We usually used a scan area of ~45 × ~22 nm^2 with (100–150) × (50–75) pixels. The AFM images were captured at frame rates of 10–12.5 fps. After taking images, we tracked a target molecule using two-dimensional (2D) correlation analysis to compensate for the slow drift of the sample stage position in the x- and y-directions. A 3 × 3 pixel-average filter was applied to each tracked image to reduce noise. For the AFM images obtained under nucleotide-free and AMPPNP conditions in which the conformational change does not occur, frame averaging was applied before the pixel averaging (Fig. S2). The AFM images were displayed first with black-to-white color scale and then the color scale was nonlinearly assigned to the height level to highlight the top-surface structure (Fig. S4).

Correlation analysis

To determine the time evolution of the conformational state of each β subunit, we calculated a 2D correlation coefficient for its image in the following way. As shown in Fig. S7, for each β we arbitrarily chose a reference frame and a region of interest (ROI) so that the ROI in the reference frame fully contained an open-state β subunit. The 2D correlation coefficient defined below was calculated frame-by-frame for each ROI. For images obtained in AMPPNP, we chose a closed- or open-state β subunit as the reference. The 2D correlation coefficient is defined as,

$$r = \frac{\sum_m \sum_n (H_{mn} - \bar{H})(R_{mn} - \bar{R})}{\sqrt{(\sum_m \sum_n (H_{mn} - \bar{H})^2)(\sum_m \sum_n (R_{mn} - \bar{R})^2)}}$$

Here, H_{mn} and R_{mn} are heights at pixel point (m, n) in a to-be-analyzed ROI and a reference ROI of the reference frame, respectively. $\bar{H}$ and $\bar{R}$ are mean values of the

height matrices H and R, respectively.

Measurement of cumulated number of CCO shifts

As mentioned in the main text, the most populated conformational state was the CCO state, in which one β subunit is in the open (O) state and the other two are in the closed (C) state. The other conformational states (COO, CCC, OOO) were much less frequent and therefore considered to be unusual conformations. To reveal unidirectional propagation of the conformational states, we defined the cumulated number of the CCO shifts (N_{CCO}) as follows. When the CCO state first appears in successive AFM images, N_{CCO} is set to be 1. Then, when the CCO state shifts counterclockwise, N_{CCO} is increased by 1. In contrast, when the CCO state shifts clockwise, N_{CCO} is reduced by 1. Here, unusual states are ignored and therefore do not affect N_{CCO}. This counting was carried out for all consecutive frames.

Measurement of cumulated rotational angle

The open-state β had a higher protrusion than that of the closed-state β (Fig. 1). We obtained the pixel position that has the highest intensity in each frame (P), and tracked such positions in consecutive images (see inset of Fig. 2B). The averaged position of the tracked highest-intensity positions was defined as the center (O). The cumulated rotational angle of the $\overrightarrow{OP}$ relative to the vector $\overrightarrow{OP}$ in the first frame was then calculated.

Calculation of the degree of underestimation of unidirectionality

In the experiment shown in Fig. 2 and 3, the frame capture time (t) was 80 ms and the time constant (τ) of the open state at 2 μM ATP was 0.66 s (Fig. S11) irrespective of counterclockwise or clockwise shift. Assuming a Poisson process, the probability ($P(N)$) that the shifts occur N-times within the frame capture time can be calculated by following equation.

$$P(N) = (1/N!) \times (t/\tau)^N \times \exp(-t/\tau)$$

Thus, the probability of single clockwise shift within the frame capture time is $(1/1)\times(0.08/0.66)\times\exp(-0.08/0.66) = 0.107$, and that of two consecutive counterclockwise shifts is $(1/2)\times(0.08/0.66)^2\times\exp(-0.08/0.66) = 0.0065$. Using these values, fraction of the two consecutive counterclockwise shifts included in the apparent single clockwise shift was estimated to be $\{0.0065/(0.0065+0.107)\} \times 100 = 5.7\%$.

Simulation of AFM image

We used software (SPM simulator, Advanced Algorithm Systems Co., Tokyo, Japan) to simulate AFM images of the $\alpha_3\beta_3$ attached to a substrate surface at either the C- or N-terminal side. The simulation was carried out with a simple hard-sphere model. The cantilever tip was modeled as a circular cone (apex angle, 10°) with a small sphere (radius, 0.5–2 nm) at the apex. Crystal structures of the nucleotide-free $\alpha_3\beta_3$ subcomplex (PDB code, 1SKY) and nucleotide-bound $\alpha_3\beta_3\gamma$ subcomplex (PDB code: 1BMF) were used as the samples. For the latter case, the γ subunit was removed from the crystal structure. Each atom in the protein was modeled as a hard sphere with a corresponding van der Wars radius. We simulated AFM images using various radii for the tip-apex sphere and found that a radius of 0.5 nm produced the images most similar to the actual AFM images. The simulated images were processed by a low-pass filter with a cut-off wavelength of 2 nm, because the spatial resolution of the AFM image was approximately 2 nm judging from the 2D Fourier transformation of actual AFM images.

LEGENDS FOR SUPPORTING FIGURES

Fig. S1. Purification and ATPase activity of $\alpha_3\beta_3$ subcomplex. (A) SDS-PAGE of purified $\alpha_3\beta_3$ and $\alpha_3\beta_3\gamma$ subcomplexes. (B) ATP hydrolysis rate of $\alpha_3\beta_3$ as a function of ATP concentration. The rate obeyed Michaelis-Menten kinetics (solid line), yielding a Michaelis constant (K_m) of 12 μM and a maximum velocity (V_{max}) of 12 s^{-1}.

Fig. S2. Comparison of raw, temporally filtered, and spatially filtered AFM images. (A), (B), and (C) correspond to the raw, frame-averaged (22 frames), and 3 × 3 pixel-averaged images obtained without nucleotide, respectively. Scan range, 16 nm × 16 nm. Pixel numbers, 46 pixels × 46 pixels. (D) and (E) correspond to the raw and pixel-averaged images in 2 μM ATP. Scan range, 14 nm × 14 nm. Pixel numbers, 32 pixels × 32 pixels.

Fig. S3. Wide-area AFM images of $\alpha_3\beta_3$ subcomplex without nucleotide and in 2 mM ATP. Frame rate, 1 fps. Scale bar, 20 nm. (A) An AFM image without nucleotide. In this image, all molecules show a pseudo-six-fold symmetric ring shape in which three βs in the ring are in the open state. (B) An AFM image in 2 mM ATP. Because the rate of conformational change was high in this ATP concentration as compared with the

frame rate of observation, all molecules showed a triangle shape in which βs in the ring are almost in the closed state (66% of a frame capture time) during scanning. These results indicate that almost all of $\alpha_3\beta_3$ molecules behave in the same way and show different conformations depending on the presence and absence of ATP.

Fig. S4. Three dimensional illustrations of the crystal structure and AFM image in nucleotide-free condition. The α and β subunits of the crystal structure are colored in cyan and pink, respectively. The C-terminal DELSEED motif of β corresponding to the high protruding portions is highlighted in red. The color scale to display the AFM image is not linearly set for the height level. This is because the height of $\alpha_3\beta_3$ is about 9 nm but the height variation at the top-most surface is less than 1 nm. To highlight the top-most structure contained in the AFM image, the complete dark scale is used for the height regions from the bottom to 80% of the highest position. Above this threshold, a linear brightness scale is used.

Fig. S5. Experimental and simulated AFM images of the N-terminal side of $\alpha_3\beta_3$ subcomplex (Online movie S2). (A) An AFM image experimentally obtained without nucleotide. (B) N-terminal side of the atomic structure of $\alpha_3\beta_3$ subcomplex (PDB code: 1SKY). The α and β subunits are colored in cyan and pink, respectively. (C) Simulated AFM image constructed from the atomic structure (PDB code: 1SKY).

Fig. S6. Tight correlation between two types of conformational changes in β observed in ATP; different heights of protrusion ("H," high; "L," low) and open (O)/closed (C) conformations of the distal region. The higher protrusion is mostly accompanied by the open conformation, whereas the lower protrusion is mostly accompanied by the closed conformation.

Fig. S7. Reference AFM images and regions of interest (ROIs) used in the correlation coefficient analysis of β conformations observed in ATP (results shown in Fig. 2). The transparent boxes show ROIs. The image of β in each ROI appears to be in the open state.

Fig. S8. Correlation coefficient analysis of three βs in $\alpha_3\beta_3$ subcomplex observed in nucleotide-free condition. (A) AFM image of $\alpha_3\beta_3$. (B) Reference images and ROIs used in the correlation analysis. For each β, an arbitrary image was chosen as the reference image. (C) Correlation coefficient distributions for the three βs. (D) Time

courses of correlation coefficient for three βs.

Fig. S9. Correlation coefficient analysis of three βs in $\alpha_3\beta_3$ subcomplex observed in AMPPNP. (A) AFM image of $\alpha_3\beta_3$. (B) Reference images and ROIs used in the correlation analysis. Reference images were chosen so that β_1 appears to be in the open state whereas β_2 and β_3 appear to be in the closed state. (C) Correlation coefficient distributions for the three βs. (D) Time courses of correlation coefficient for the three βs.

Fig. S10. Distributions of the number of successive shifts of the "CCO" state in clockwise (top) and counterclockwise (bottom) directions. Distributions at (A) 2 μM, (B) 3 μM, and (C) 4 μM ATP. The direction of the "CCO" shift is clearly biased in the counterclockwise direction. The values for "mean" indicate the average number of successive shifts, and the values for "s.d." indicate the standard deviations.

Fig. S11. Histograms of dwell times for the open (top) and closed (bottom) states in various concentrations of ATP (A: 2 μM, $n = 266$; B: 3 μM, $n = 426$; C: 4 μM, $n = 374$). Dwell time distributions for the open state are well fitted with single exponential decay functions (solid lines on top). The distributions for the closed state are fitted with functions representing consecutive reactions with two identical time constants:
$A \times t \times \exp(-t/\tau)$ (solid lines on bottom).

Fig. S12. Loss of a single subunit stops rotary propagation of conformational changes. (A and D) AFM images before and after loss of β_1 (A) or α_1 (D) (Online movies S7 and S8). (B and E) Time courses of correlation coefficients for the three βs designated in (A) and (D), respectively. Solid horizontal lines show the mean correlation coefficients for the periods of open and closed states. The states are judged by examining whether the correlation coefficients are above or below a threshold (0.978). β_1 (B) is lost at 16.2 s and α_1 (E) is lost at 9.4 s (vertical broken lines). (C and F) Cumulated angles of open β measured using the highest pixel position in each frame. [ATP], 2 μM; frame rate, 12.5 fps.

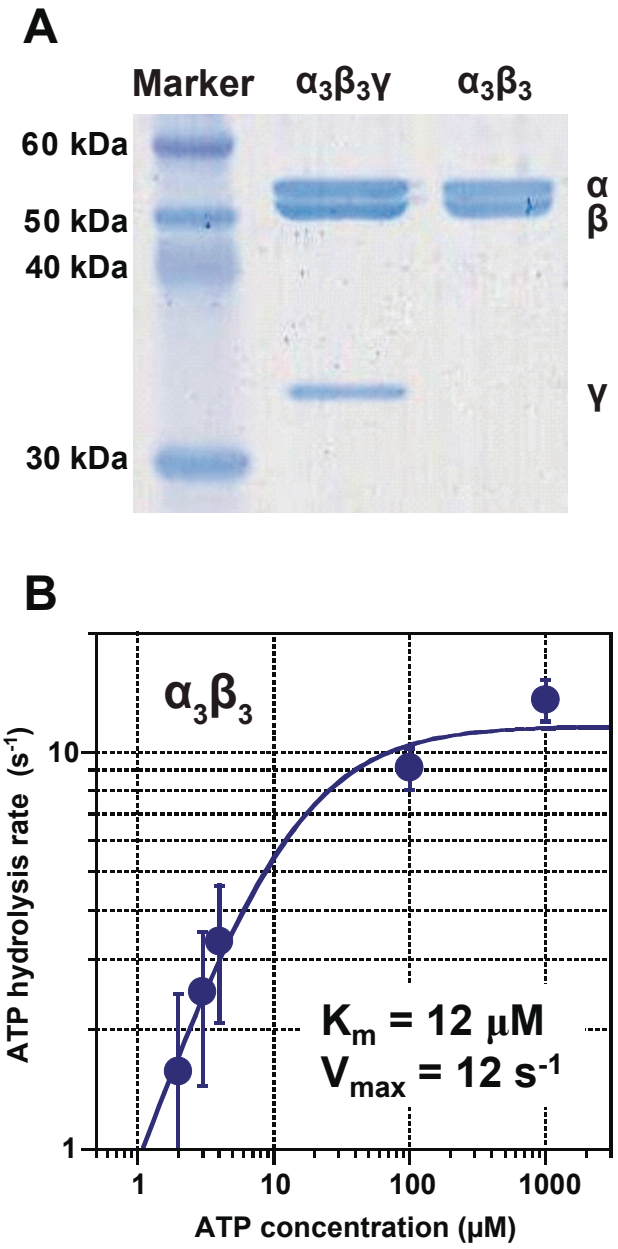
A
Marker
α3β3γ
α3β3
60 kDa
50 kDa
40 kDa
30 kDa
α
β
γ
B
α3β3
ATP hydrolysis rate (s-1)
10
1
Km = 12 μM
Vmax = 12 s-1
1
10
100
1000
ATP concentration (μM)

Fig. S1

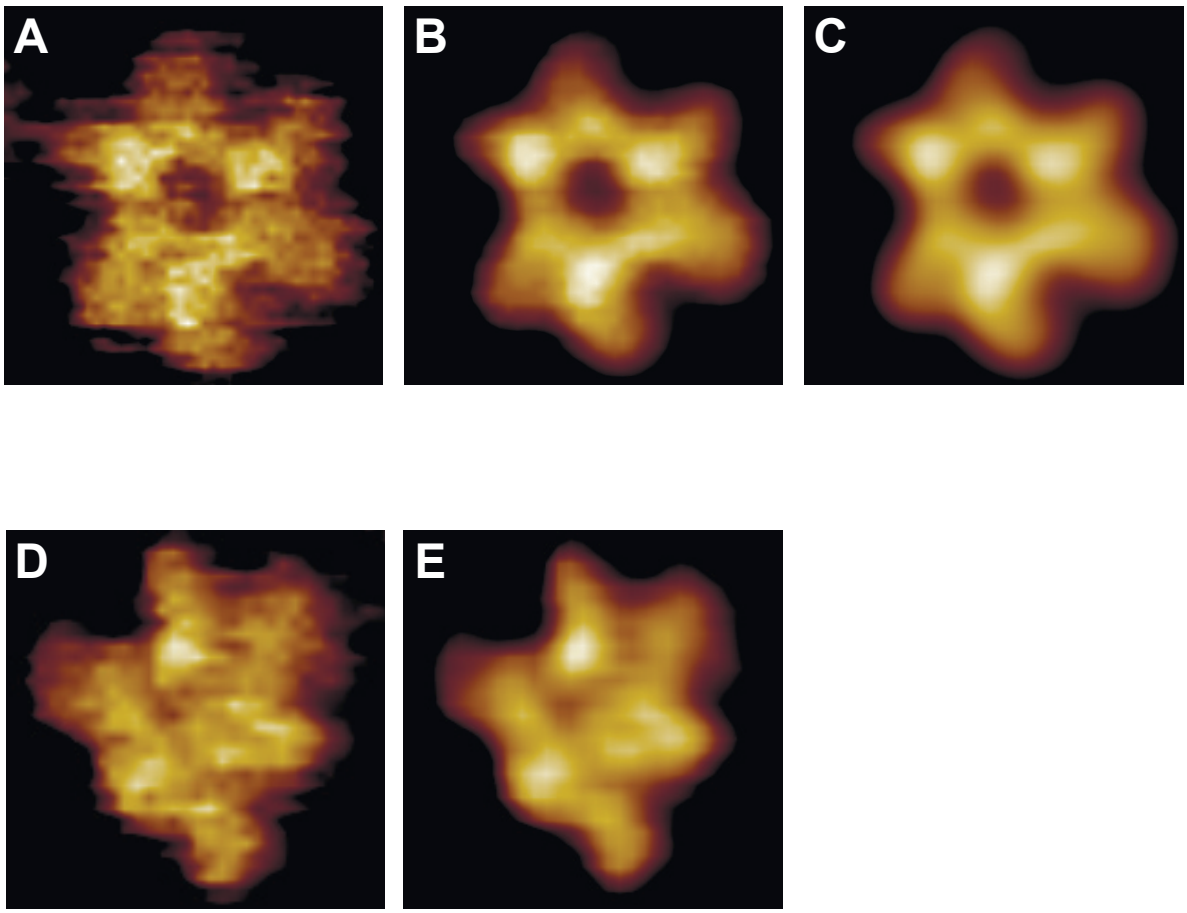

Fig. S2

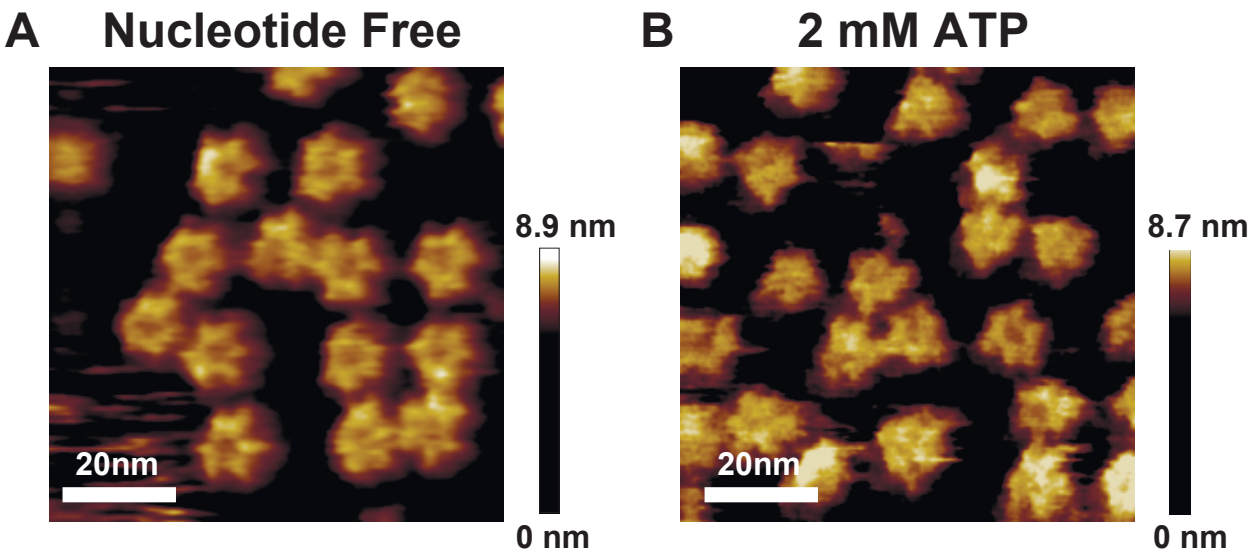

Fig. S3

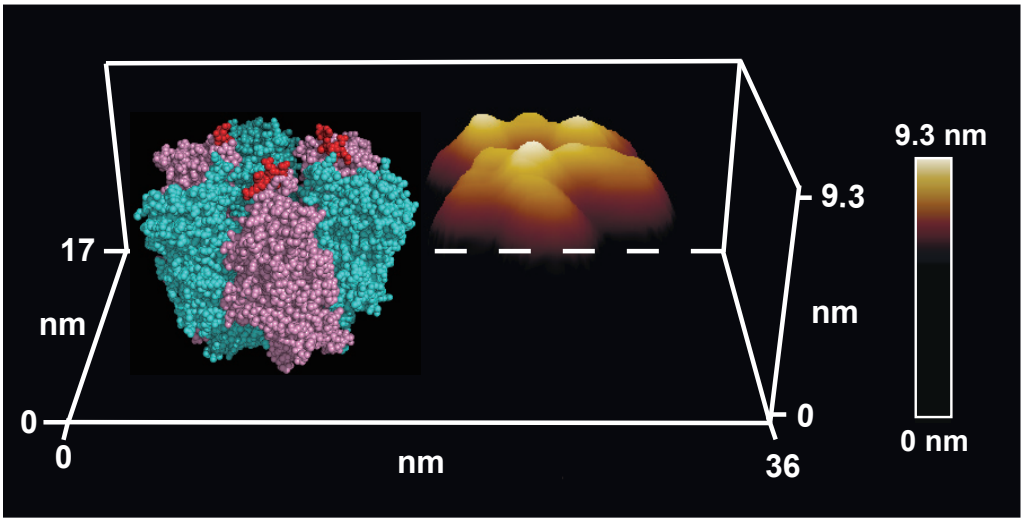

Fig. S4

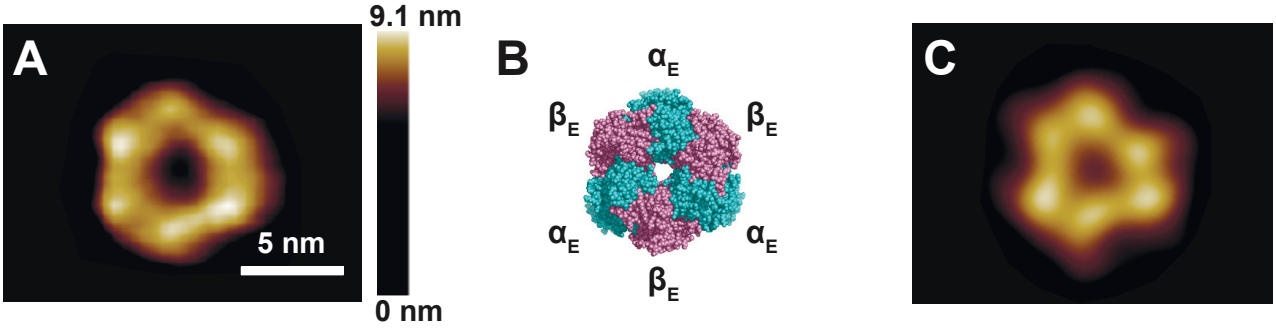

Fig. S5

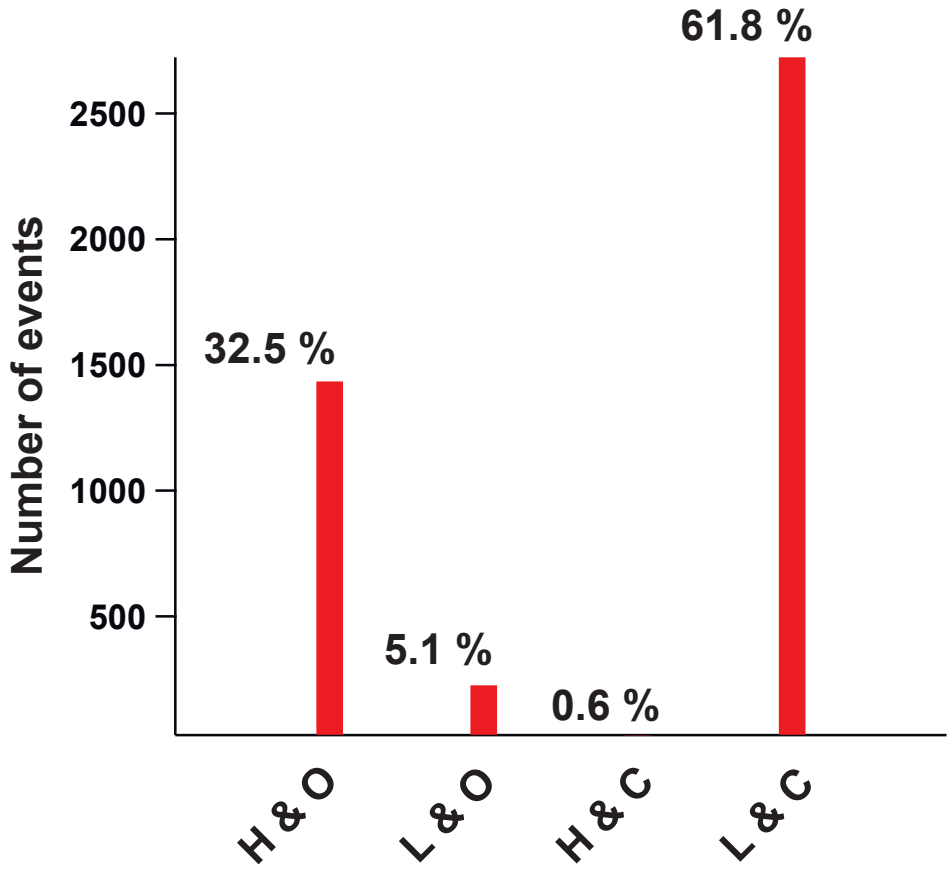
61.8 %
2500
2000
Number of events
1500
32.5 %
1000
500
5.1 %
0.6 %
H&O
L&O
H&C
L&C

Fig. S6

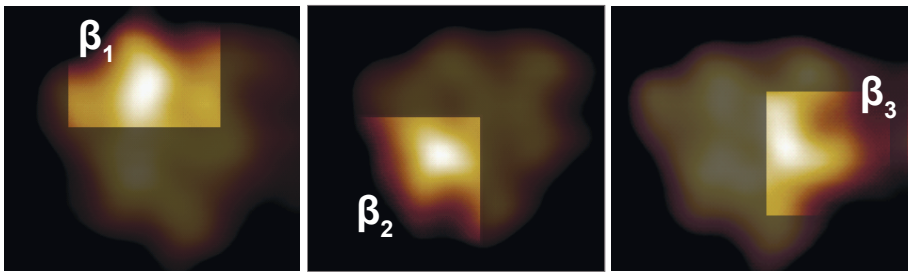

Fig. S7

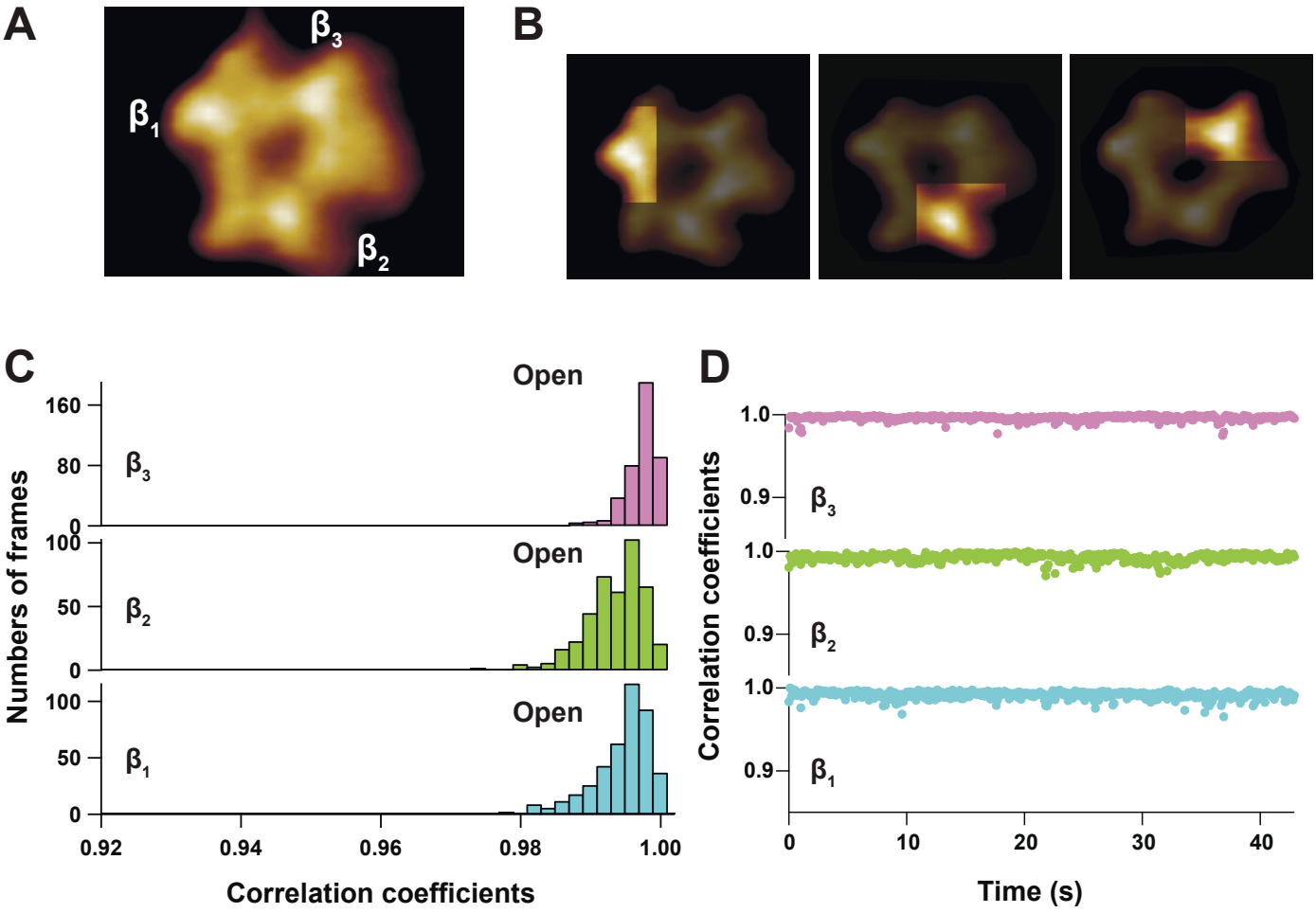
A
β3
β1
β2
B
C
Open
160
80
0
β3
100
50
0
β2
100
50
0
β1
Numbers of frames
0.92
0.94
0.96
0.98
1.00
Correlation coefficients
D
1.0
0.9
β3
β2
β1
Correlation coefficients
0
10
20
30
40
Time (s)

Fig. S8

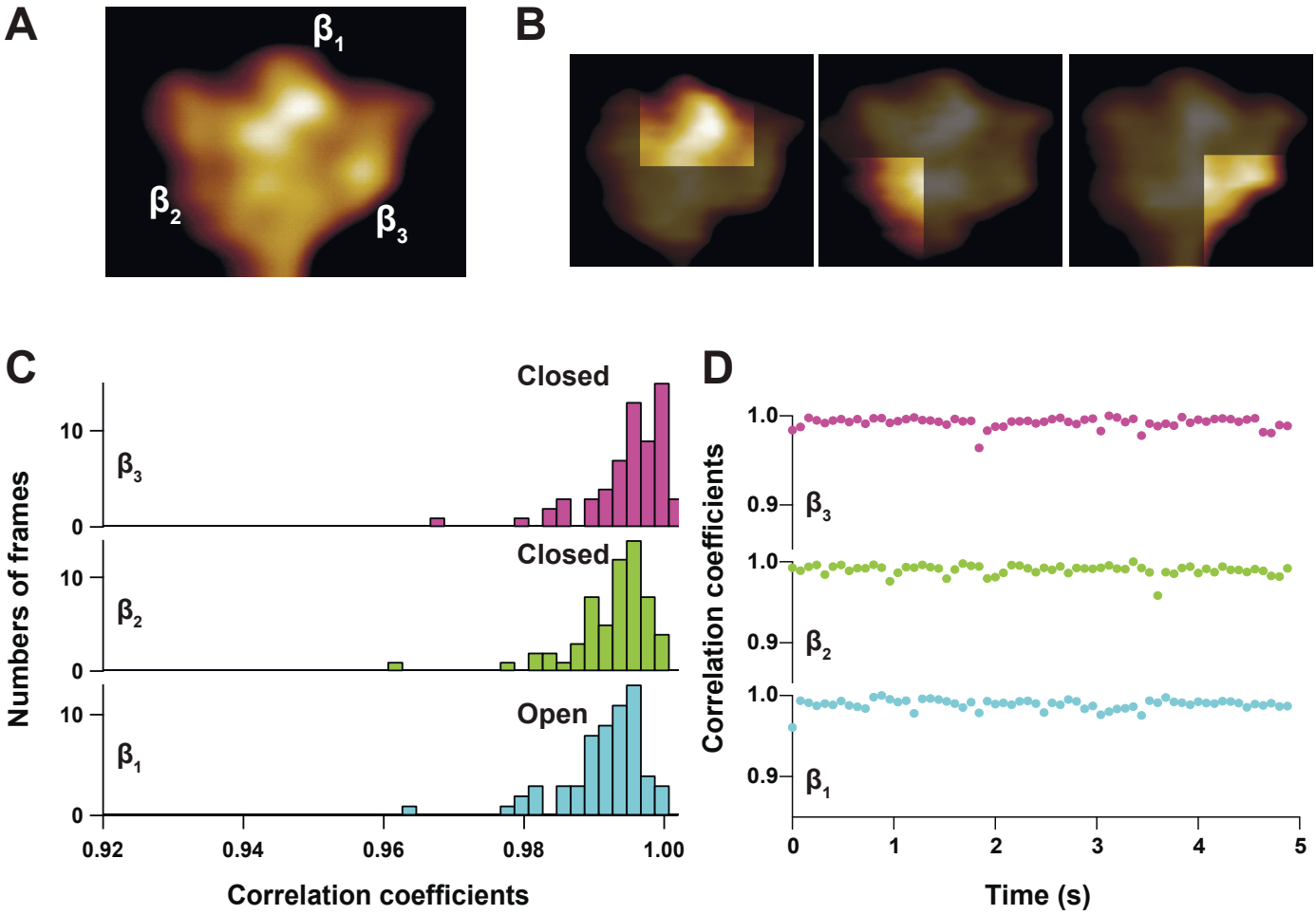
A
β1
β2
β3
B
C
Closed
Closed
Open
β3
β2
β1
10
0
Numbers of frames
0.92
0.94
0.96
0.98
1.00
Correlation coefficients
D
1.0
0.9
Correlation coefficients
0
1
2
3
4
5
Time (s)

Fig. S9

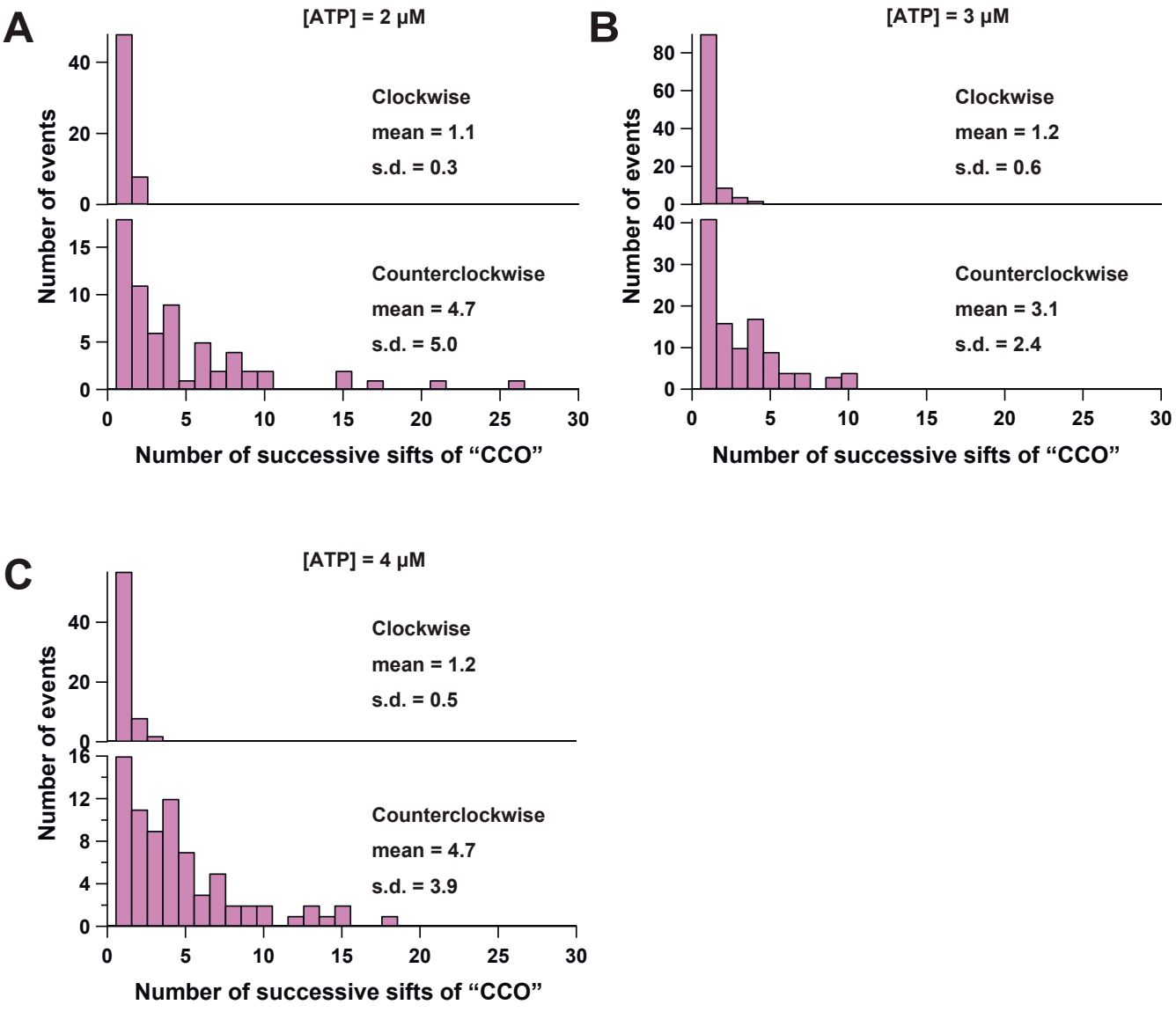
A
[ATP] = 2 μM
Clockwise
mean = 1.1
s.d. = 0.3
Counterclockwise
mean = 4.7
s.d. = 5.0
Number of events
Number of successive sifts of "CCO"
B
[ATP] = 3 μM
Clockwise
mean = 1.2
s.d. = 0.6
Counterclockwise
mean = 3.1
s.d. = 2.4
Number of events
Number of successive sifts of "CCO"
C
[ATP] = 4 μM
Clockwise
mean = 1.2
s.d. = 0.5
Counterclockwise
mean = 4.7
s.d. = 3.9
Number of events
Number of successive sifts of "CCO"

Fig. S10

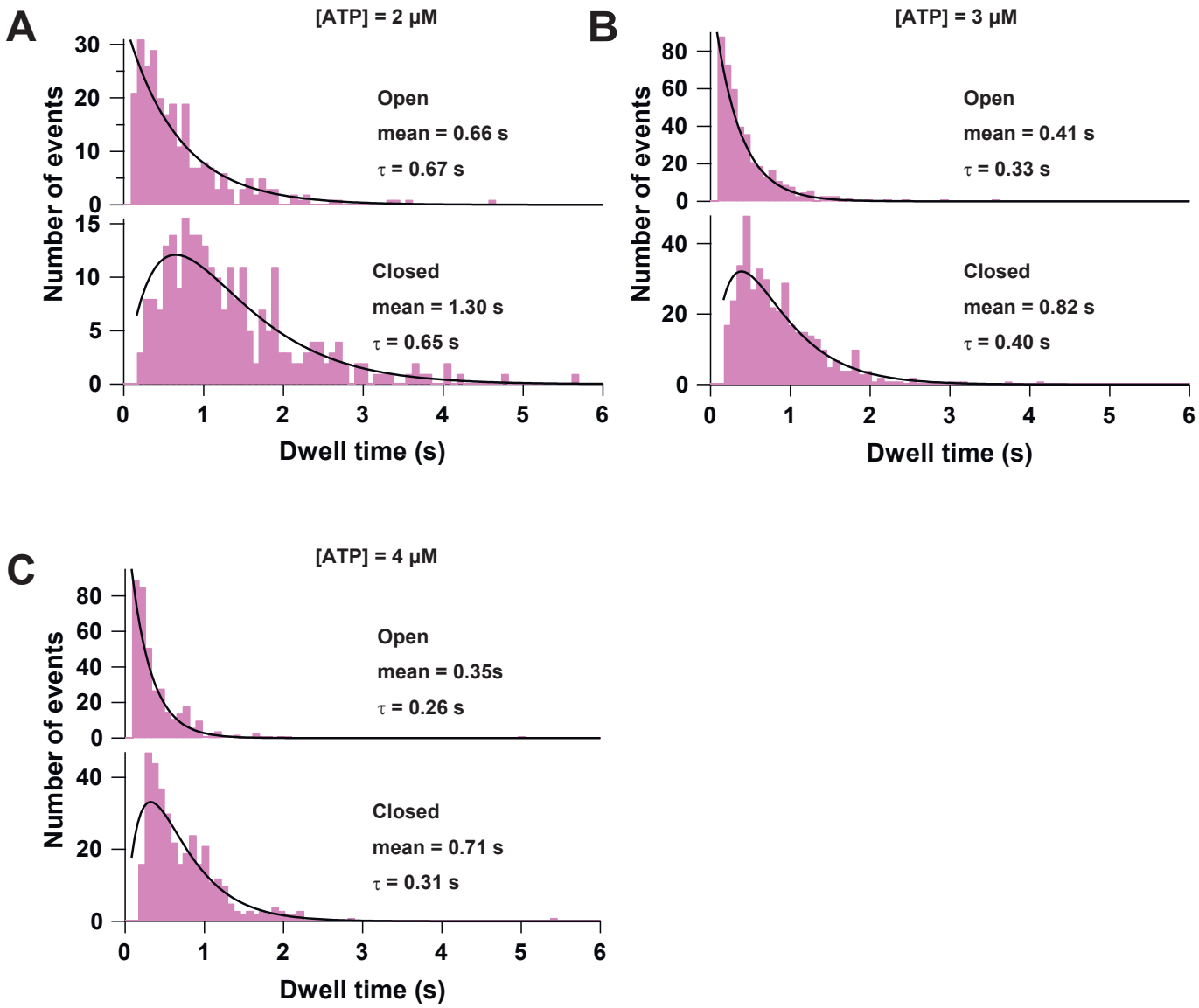
A
[ATP] = 2 μM
Open
mean = 0.66 s
τ = 0.67 s
Closed
mean = 1.30 s
τ = 0.65 s
Number of events
Dwell time (s)
B
[ATP] = 3 μM
Open
mean = 0.41 s
τ = 0.33 s
Closed
mean = 0.82 s
τ = 0.40 s
Number of events
Dwell time (s)
C
[ATP] = 4 μM
Open
mean = 0.35s
τ = 0.26 s
Closed
mean = 0.71 s
τ = 0.31 s
Number of events
Dwell time (s)

Fig. S11

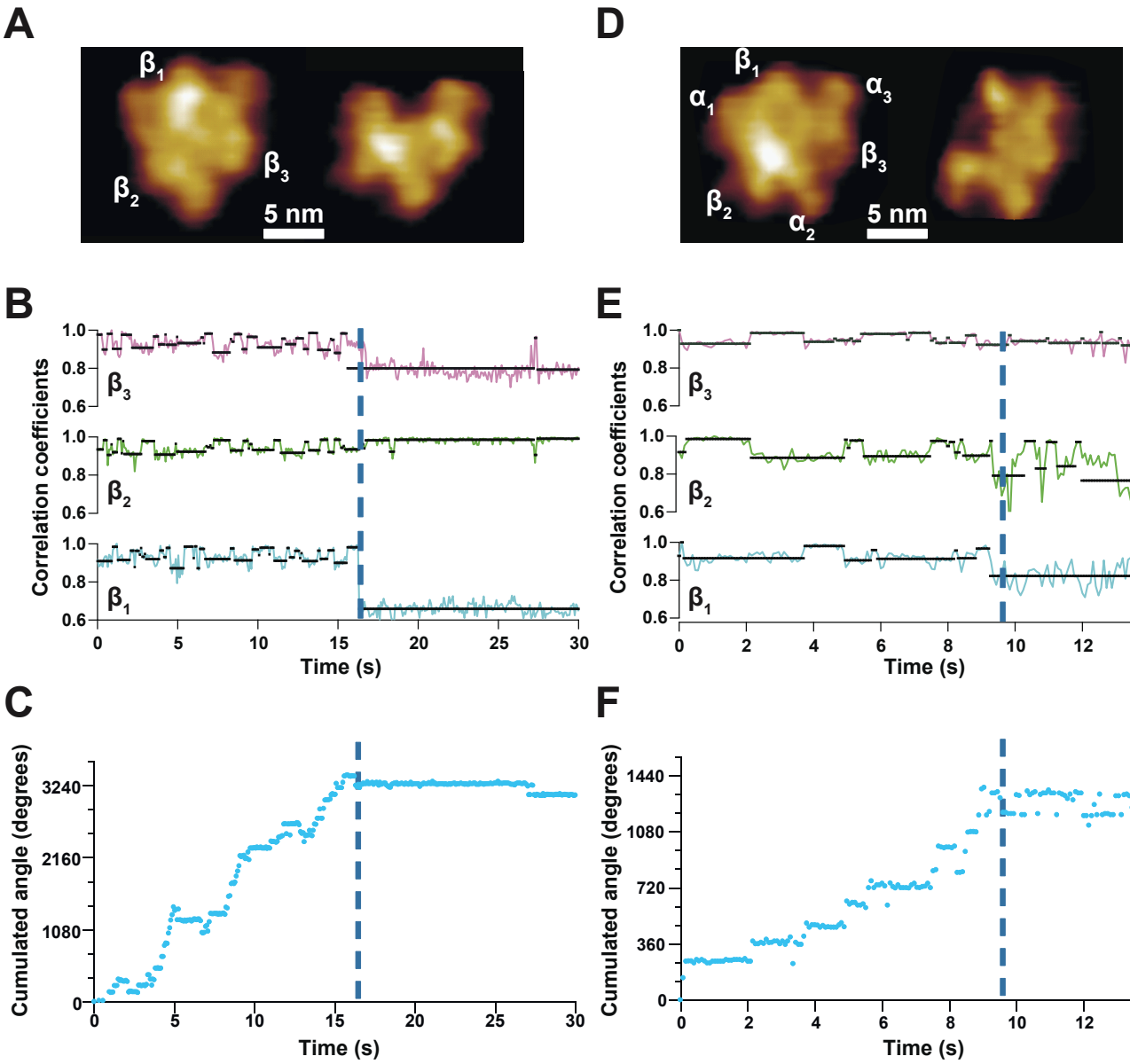
A
β1
β2
β3
5 nm
D
β1
α1
α3
β3
β2
α2
5 nm
B
Correlation coefficients
β3
β2
β1
Time (s)
E
Correlation coefficients
β3
β2
β1
Time (s)
C
Cumulated angle (degrees)
Time (s)
F
Cumulated angle (degrees)
Time (s)

Fig. S12

Table S1. Fraction of molecules showing conformational changes under various nucleotide conditions.

Nucleotide conditions	Number of observed molecules	Number of change-detected molecules	Fraction of change-detected molecules
Nucleotide-free	53	0	0%
1 mM AMPPNP	46	0	0%
2 μM ATP	95	90	89%
3 μM ATP	86	81	94%
4 μM ATP	64	62	97%